Research
Green Chemical Engineering—Article

Engineering Sodium Metal Anode with Sodiophilic Bismuthide Penetration for Dendrite-Free and High-Rate Sodium-Ion Battery

Wanyu Zhao [a], Min Guo [b], Zhijun Zuo [c], Xiaoli Zhao [a], Huanglin Dou [a], Yijie Zhang [a], Shiying Li [a], Zichen Wu [a], Yayun Shi [c], Zifeng Ma [d,*], Xiaowei Yang [a,d,*]

[a] Key Laboratory of Advanced Civil Engineering Materials of Ministry of Education, School of Materials Science and Engineering, Tongji University, Shanghai 201804, China
[b] School of Chemistry and Chemical Engineering, Shaoxing University, Shaoxing 312000, China
[c] Key Laboratory of Coal Science and Technology of Ministry of Education and Shanxi Province, Taiyuan University of Technology, Taiyuan 030024, China
[d] Shanghai Electrochemical Energy Devices Research Center, School of Chemistry and Chemical Engineering, Shanghai Jiao Tong University, Shanghai 200240, China

A R T I C L E   I N F O

A B S T R A C T

Sodium (Na) metal batteries with a high volumetric energy density that can be operated at high rates are highly desirable. However, an uneven Na-ion migration in bulk Na anodes leads to localized deposition/dissolution of sodium during high-rate plating/stripping behaviors, followed by severe dendrite growth and loose stacking. Herein, we engineer the Na hybrid anode with sodiophilic Na_3Bi-penetration to develop the abundant phase-boundary ionic transport channels. Compared to intrinsic Na, the reduced adsorption energy and ion-diffusion barrier on Na_3Bi ensure even Na^+ nucleation and rapid Na^+ migration within the hybrid electrode, leading to uniform deposition and dissolution at high current densities. Furthermore, the bismuthide enables compact Na deposition within the sodiophilic framework during cycling, thus favoring a high volumetric capacity. Consequently, the obtained anode was endowed with a high current density (up to 5 mA·cm^{-2}), high areal capacity (up to 5 mA·h·cm^{-2}), and long-term cycling stability (up to 2800 h at 2 mA·cm^{-2}).

1. Introduction

Rechargeable batteries with high volumetric energy densities that can be charged/discharged at high rates are desirable for electric vehicles (EVs) and other high-power devices [1–5]. While considerable progress has been achieved in the most commercialized lithium-ion batteries, depleted Li resources remain a significant issue for market consideration [6–10]. Na-ion batteries offer an affordable and earth-abundant alternative to Li counterpart [11–13]; however, the commonly used hard carbon anodes with high-rate features suffer the suboptimal energy densities [14–16]. Na with a low electrochemical potential and high theoretical capacity is considered a promising anode material [17–21]. However, dendrite growth and loose deposition stacking remain the major barriers impeding the application of Na anodes in engineering, especially at high rates [22–32].

The formation of dendrites on Na anodes stems from uneven ion distribution and electrodeposition [33,34]. An ideal Na deposition at high current densities requires rapidly and evenly distributed Na^+ flux. Otherwise, Na^+ would prefer to selectively electrodeposite on local sites, causing dendrite or porous stacking growth [35]. During the stripping process, Na ions have to migrate from the interior of the bulk Na anodes into the electrolyte [36,37]. Nevertheless, Na in the dense metal foil primarily diffuses through sluggish lattice diffusion (10^{-9} cm^2·s^{-1}) with a high Na^+ diffusion barrier [37–41], thus possibly leading to the localized dissolution of metallic Na during the high-rate stripping process, followed by the collapse of local solid electrolyte interphase (SEI) layer, and then triggering dendrite growth in the following plating process [37]. To address the above issues, tactics of introducing ionic transport paths with a low Na^+ diffusion barrier is conducive to accelerate the Na diffusion throughout the bulk anodes. Although complex electrodes with mixed ion and electron-conducting scaffolds have been reported in recent studies, commonly using porous structures may result in irreversible electrolyte consumption and low volumetric capacity [25,42–46]. The balance between the fast

---

* Corresponding authors.
  E-mail addresses: zfma@sjtu.edu.cn (Z. Ma), yangxw@tongji.edu.cn (X. Yang).

charge/discharge, dendrite-free deposition, and compact stacking remains challenging.

Here, we introduced "sodiophilic" Na$_3$Bi penetration into Na anodes to build abundant phase-boundary ion-transport channels. Ion diffusion along the phase boundaries is supposed to enable several orders of magnitude faster than lattice diffusion [41,47–49]. Thus, Na ions quickly extract/insert along the boundaries between Na and Na$_3$Bi phase during stripping and plating processes, thus maintaining the even ion-flux distribution as shown in Fig. 1(a). Moreover, the sodiophilic bismuthide enables uniform and dense Na deposition during cycling, thus aiding high volumetric capacity. The Na$_3$Bi-penetrated Na hybrid anode delivers a high current density of 5 mA·cm^{-2} along with a capacity of 5 mA·h·cm^{-2} for over 300 h and ultralong cycle life (over 2800 h) at 2 mA·cm^{-2} under 2 mA·h·cm^{-2}. The Na$_3$V$_2$(PO$_4$)$_3$ (NVP)/(Na/Na$_3$Bi) full cell exhibits superior electrochemical performance than those with the bare Na foil anodes.

2. Results and discussion

Fig. 1 shows the comparison between Na$_3$Bi-penetrated Na and Na on Cu foil (Na/Cu anode) during initial plating, subsequent stripping, and plating behaviors. During predepositing Na on Cu foil, Na$^+$ flux preferentially deposits at tips because of the convergent electrical field, thus forming non-uniform initial deposition (Fig. 1(b)). The sluggish and uneven Na$^+$ diffusion paths lead to localized dissolution and deposition over cycling in subsequent stripping and plating processes. The resulting cavities and volumetric fluctuations induce continuous destruction and repair of the SEI, thus becoming a potential danger of dendrite growth. Conversely, Na$^+$ flux nuclear homogenously on the Na$_3$Bi framework for the initial plating because of the strong affinity between Na and Na$_3$Bi, thereby filling the inner space of the Na$_3$Bi framework (Fig. 1(a)) to ensure the compactness of Na$_3$Bi-penetrated Na hybrid anode and deliver high volumetric capacity. Correspondingly, Na$^+$ rapidly exits/enters along the boundaries, thus maintaining the stability of the anode interface. Unlike the Na/bulk Na$_3$Bi anode, although because of the sodiophilic nature of the Na$_3$Bi material, bulk Na$_3$Bi can lead to uniform deposition to some certain extent. However, because of the lack of a framework to accommodate metallic Na, it tends to concentrate on the upper part of the anode, which is not conducive to long-term cycle stability (Scheme S1 in Appendix A).

The compact Na anodes with Na$_3$Bi penetration (Na/Na$_3$Bi anode) was developed by electroplating metallic Na into a three-dimensional (3D) Na$_3$Bi framework. The Na$_3$Bi framework was evolved from bismuth (Bi) powder through alloying/dealloying processes (Figs. S1 and S2 in Appendix A) [50,51]. Fig. 2(a) shows the scanning electron microscopy (SEM, Nova NanoSEM450, FEI company, USA) image. The Na$_3$Bi framework presents a coral-like structure, and the unique morphology makes it easier for Na$^+$ to be deposited uniformly (Fig. 2(b), as described later). In a high-resolution transmission electron microscope (HRTEM, JEM-2100, JEOL, Japan) image (Fig. S3 in Appendix A), the interplanar distance of 4.04 Å (1 Å = 10^{-10} m) corresponded to (101) crystal planes of Na$_3$Bi. After electroplating, metallic Na is completely embedded in the Na$_3$Bi framework to form the Na$_3$Bi-penetrated Na anodes, as shown in Figs. 2(c) and (d). The prominent peaks in the X-ray diffraction (XRD, D8 Advance, Bruker, Germany) spectra are well matched to the characteristic Na$_3$Bi and Na, confirming that the presence of Na does not affect the composition of the framework (Fig. S4 in Appendix A). We set up two control groups, namely, the Na/bulk Na$_3$Bi (i.e., without the alloying/dealloying process and framework structure) and Na/Cu anodes, to compare the superiority of the Na/Na$_3$Bi anode. Furthermore, the difference between the control groups is described in detail in Appendix A.

The "sodiophilic" Na$_3$Bi framework leads to uniform local ion distribution and delivers homogenous inner-space Na$^+$ plating. The energy to overcome the nucleation barrier between Na and substrates is remarked as a nucleation overpotential. As shown in Figs. 2(b) and S5 in Appendix A, the overpotential on Cu is ~19 mV at 0.1 mA·cm^{-2} and ~20 mV at 1 mA·cm^{-2}, whereas Na$_3$Bi framework and bulk Na$_3$Bi show an extremely small overpotential (below 4 mV) at the same current density. Differences became apparent with increase in current (Fig. S6 in Appendix A). Thus, both bulk Na$_3$Bi and Na$_3$Bi framework samples effectively reduce the nucleation overpotential, thus confirming the sodiophilic nature of Na$_3$Bi. The same conclusion could be drawn in
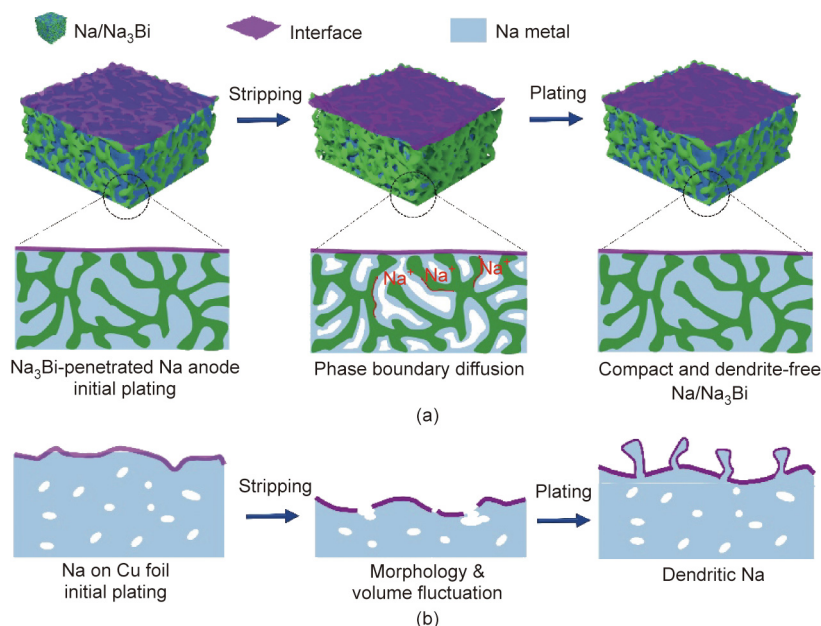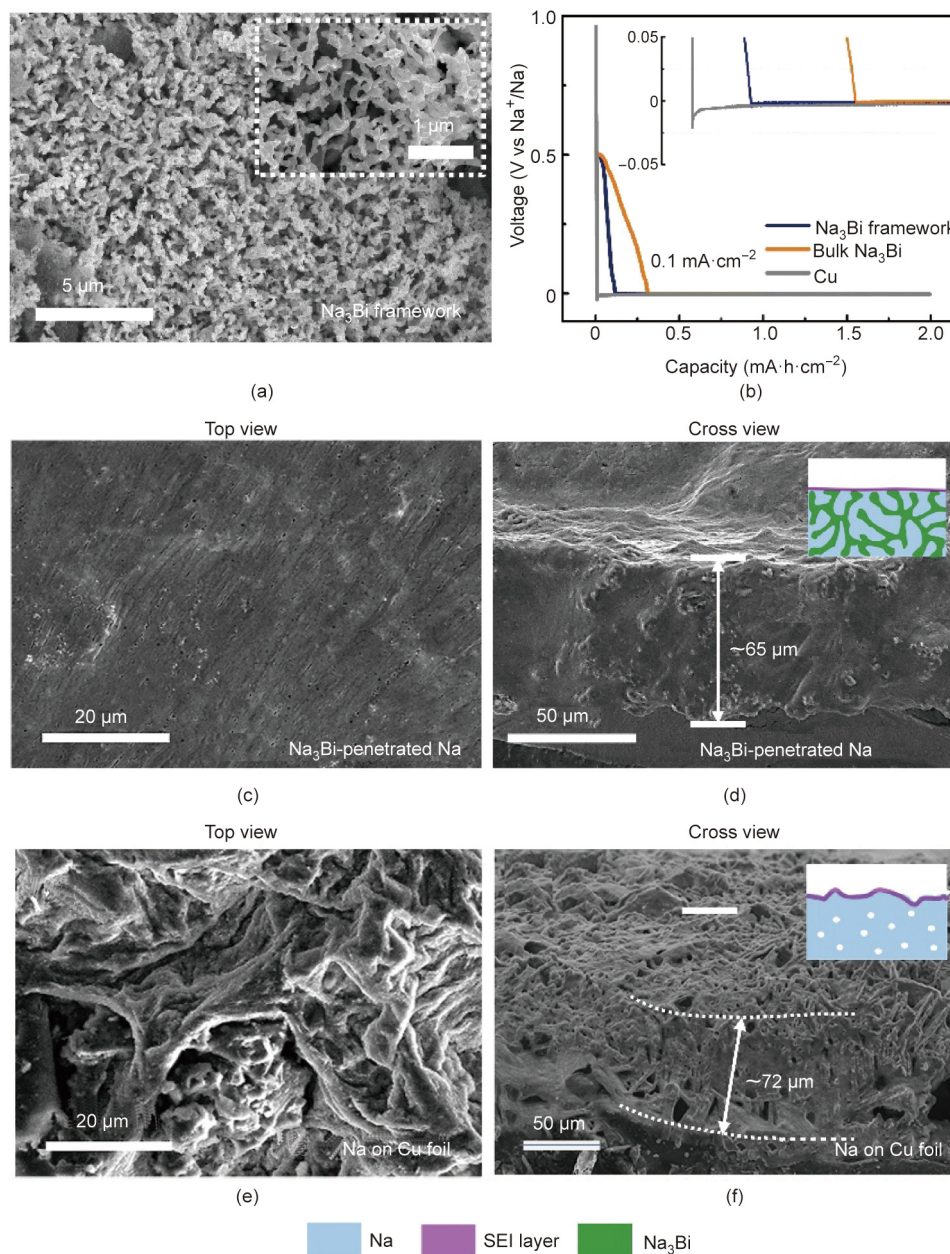

Fig. 1. Schematic for Na stripping/plating in (a) Na$_3$Bi-penetrated Na and (b) Na/Cu anode.

Fig. 2. (a) SEM images of the Na₃Bi framework before penetrating in Na anode. (b) Na plating curves on three matrix samples at 0.1 mA·cm⁻², showing overpotential of Na nucleation. SEM images of top and cross view of (c, d) compact Na anodes with Na₃Bi penetration and (e, f) Na on Cu foil. The insets schematically elucidate the initial plating morphology.

the phase diagram where Na–Bi alloy exists, and there is no solubility for Na–Cu at room temperature (Fig. S7 in Appendix A), confirming that lower nucleation barriers are present on Na₃Bi [52].

Uniform and compact deposition of Na on Na₃Bi could be visually observed in SEM images. As shown in Fig. S8 in Appendix A, Na surrounds and covers the framework with even distribution and fills the original Na₃Bi framework with the increasing initial plating capacity increases (from 3 to 5 mA·h·cm⁻²). Top and cross-sectional SEM images show a smooth surface and compact cross-section at 8 mA·h·cm⁻² of capacity (Figs. 2(c) and (d)). Moreover, the corresponding energy dispersive X-ray spectrometer (EDX, Model 550i, IXRF, USA) mapping intuitively presents the uniform deposition (Figs. S9 and S10 in Appendix A). Consequently, the dense electrode structure demonstrates the close volumetric capacity to the theoretical value of bulk Na with nearly the maxi-

mum sodium capacity this framework could withstand. However, mossy and walnut-like Na could be observed on Na plating on Cu foil, which confirms the formation of dendrite growth after nucleating Na on the top of the Cu foil. Furthermore, uneven deposition results in a porous and loose structure (Figs. 2(e) and (f)), which is not conducive to subsequent anode long-term durability performance. As for bulk Na₃Bi, the deposition of Na is still non-uniform (Fig. S11 in Appendix A), confirming the importance of the penetrated sodiophilic frameworks to the uniform and dense deposition. Based on the above evidence, we demonstrated that the "sodiophilic" Na₃Bi framework is prone to induce uniform local ion distribution, thereby delivering homogenous the inner-space Na⁺ plating and suppressing volume fluctuations.

In addition to the even nucleation, the ionic diffusion barrier of pure Na and Na₃Bi was studied by using density-functional theory

(DFT) calculation. By equivalent adsorption sites, the diffusion barrier of Na$^+$ in all directions can be calculated [53,54]. Figs. 3(a) and (b) show the minimum energy path for Na diffusion on Na and Na$_3$Bi surfaces, and Figs. 3(c) and (d) show Na diffusion along with the minimum energy path among different adsorption sites. We also compared the Na$^+$ adsorption energy on different adsorption sites (Figs. 3(e), S12, and Table S1 in Appendix A). The maximum Na$^+$ adsorption energy of pure Na and Na$_3$Bi materials are −1.04 and −1.44 eV (1 eV = 1.602176 × 10^{-19} J), respectively. The reduced adsorption energy of Na$^+$ on Na$_3$Bi indicates that Na$^+$ is inclined to deposit on Na$_3$Bi, thus ensuring the uniform deposition of metallic Na on the Na$_3$Bi framework. The Na$^+$ diffusion barrier of Na$_3$Bi(110) is 0.14 eV; however, that of pure Na(100) is 0.27 eV (Fig. 3(e)). The rapid Na$^+$ transport on Na$_3$Bi(110) surface ensures phase boundaries between metallic Na and Na$_3$Bi with high Na$^+$ migration. For metallic Na, the 0.27 eV of Na$^+$ diffusion barrier guides one-dimensional growth pattern to form Na dendrites (Fig. 3(e)). Consequently, 3D boundary diffusion paths are distributed in the entire anode, as shown in Fig. 3(f). Moreover, the diffusion coefficient (D) and corresponding ionic conductivity of Na$^+$ in the Na$_3$Bi bulk phase were calculated by galvanostatic intermittent titration technique (GITT) test are 7 × 10^{-8} cm^2·s^{-1} and 9.8 × 10^{-4} S·m^{-1}, respectively (Fig. S13 in Appendix A). The high Na$^+$ diffusion coefficient indicates that Na$_3$Bi can withstand a part of Na$^+$ transportation. As shown in Fig. S14 in Appendix A, the GITT curves of Na/Na$_3$Bi||Na/Na$_3$Bi anode delivers lower overpotential compared to that of Na||Na anode, thus showing faster mass transfer kinetics of the Na/Na$_3$Bi electrode.

Electrochemical deposition/dissolution behaviors were further studied, and the top and cross-section of surface morphology were characterized (Figs. 4 and S15 in Appendix A). We notice an interesting phenomenon that no matter how the capacity of Na/Na$_3$Bi anode changes during plating or stripping, the anode surface morphology always remains uniform and flat. The comparison of SEM images between Na/Na$_3$Bi and Na/Cu anode with plating capacity of 3 and 5 mA·h·cm^{-2} clearly indicate that Na/Cu anode is accompanied by uneven deposition and dendrites formation (Figs. 4(a)–(d)). As shown in Figs. 4(e)–(j), theoretically, Na$_3$Bi could be gradually exposed with sodium capacity decreasing; however, the surface still maintains a relatively flat morphology, which indicates

that the Na stripping process is entirely carried out on the Na/Na$_3$Bi anode. In this manner, the integrity of the SEI formed on the surface is preserved and gradually stabilizes during subsequent plating and stripping. Cycled-anodes were disassembled and replaced in carbonate electrolyte containing specific Cl element to further confirm the stripping/deposition behaviors of bare Na along with Na/Na$_3$Bi anode. As shown in Fig. S16 in Appendix A, EDX elemental exhibits the strong Cl signal is distributed over the bare Na foil and the content is more than 3%, indicating the permeation of electrolyte into the interior of the anode. However, Na$_3$Bi-penetrated Na anodes maintain their dense structure with the Cl element's weak signal on the cross-section. Consequently, the SEI layer of Na/Na$_3$Bi anode remains stable, preventing the simultaneous permeation of electrolytes [44]. Theoretical volume change of "hostless" Na could reach 200% in the corresponding process (Fig. S17 in Appendix A); however, Na$_3$Bi-penetrated Na anodes with different sodium capacities could almost maintain the same thickness, conducive to stability.

The possible explanation for the flat surface is that theoretically, the metal holes during the stripping process would be left at the interface between Na and the SEI layer, which tend to submerge into the bulk of Na by diffusion. Unfortunately, lattice diffusion delivers a severe situation to atomic migration and is followed by poor Na diffusivity: The diffusivity of Na atoms in the Na metal possesses a low value of 10^{-9} cm^2·s^{-1} (25 °C) [38]. Consequently, holes accumulate at the sodium/SEI interface and lead to the concentration of large cavities when the rate of Na$^+$ extraction is higher than that of holes submergence [37], which is not beneficial for the stability of the SEI layer [36]. As for the Na$_3$Bi-penetrated Na anodes, the Na and Na$_3$Bi boundaries enable fast Na$^+$ diffusion such that the Na vacancies generating in the surface layer can be quickly filled to maintain the stability of the SEI layer and anode. Consequently, the stripping process can mobilize the Na source and help prevent SEI changes caused by the run-off of the surface sodium. As a result, the embedded Na is protected from exposure to the electrolyte, which causes low coulombic efficiency (CE) and contributes to the electrode's long-life cycling durability.

CE is an important indicator to investigate the durability of anodes [55]. The CE measurement was performed with three working electrodes (Cu foil, bulk Na$_3$Bi, and Na$_3$Bi framework) from the
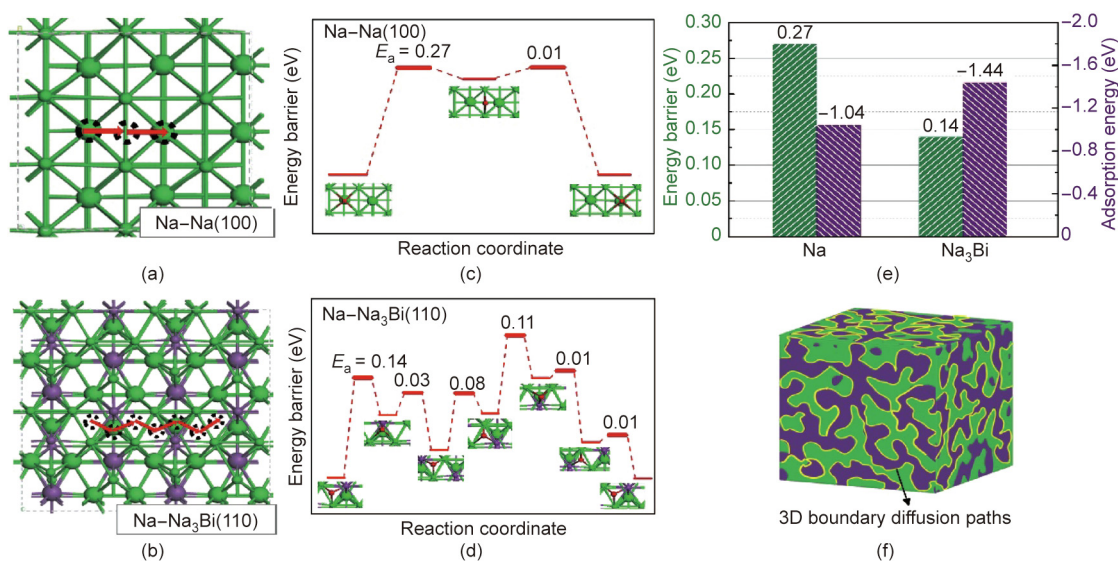
Fig. 3. The minimum energy path for Na diffusion on (a) Na and (b) Na$_3$Bi surfaces. Green and purple balls represent Na and Bi atoms. The energy barrier of Na diffusion along with the minimum energy path on (c) Na and (d) Na$_3$Bi surfaces. Red ball stands for the diffusion Na. (e) Comparison of the energy barrier of Na diffusion and adsorption energies on Na and Na$_3$Bi surfaces. (f) Schematic of 3D boundary diffusion path in Na/Na$_3$Bi anode.
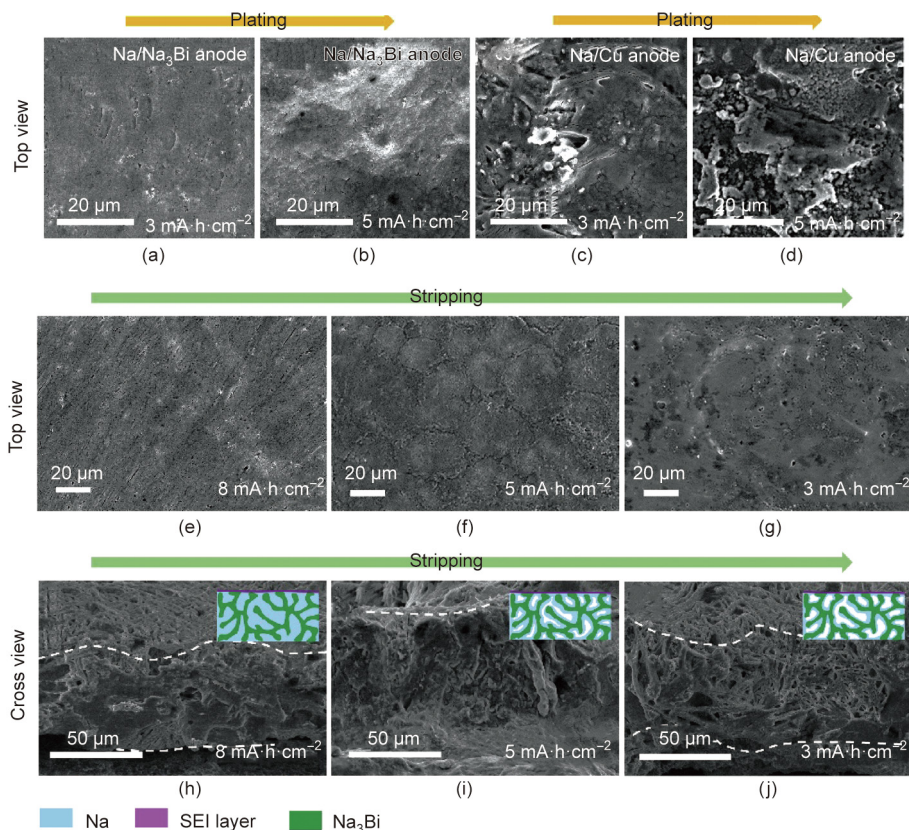
Fig. 4. Investigation of sodium plating/stripping process of Na/Na$_3$Bi and Na/Cu anode. Top view SEM images between (a, b) Na/Na$_3$Bi and (c, d) Na/Cu anode during plating process with 3 and 5 mA·h·cm^{-2}. (e–j) Top and cross view SEM images of Na/Na$_3$Bi anode during stripping process with (e, h) 8, (f, i) 5, and (g, j) 3 mA·h·cm^{-2} capacity. The inset pictures schematically elucidate the presence of sodium inside the anode.

current densities of 2–5 mA·cm^{-2} with capacities of from 2 to 5 mA·h·cm^{-2} (Figs. 5(a), 5(b), and S18 in Appendix A). Over the 900 cycles, CE of Na$_3$Bi could reach 99.78% at 2 mA·cm^{-2} and 2 mA·h·cm^{-2}, indicating SEI stability; however, Na deposition/stripping on the bulk Na$_3$Bi and Cu foil samples exhibit lower CE with high fluctuation (Fig. 5(a)). The instability of SEI could be reflected by the low CE values on Cu foil and bulk Na$_3$Bi, while the large fluctuation is attributed to the formation of dead Na and the consumption of electrolytes. The CE of Na$_3$Bi framework anode reaches 97.25% over 300 cycles when the capacity is 4 mA·h·cm^{-2}. Similar CE values and high retention exist for other current density and plating/stripping capacity (Fig. S18). The CE of Na/Na$_3$Bi anode in this study is higher than that of scaffold-constructing works and equal to that of artificial SEI-constructing works (Fig. S19 and Table S2 in Appendix A).

The nature of the interface between electrolyte components and anodes can be reflected by the Tafel plot [46,56]. Mass transfer dominants current density in high overpotential areas. The higher exchange current density (1.2 compared with 0.058 mA·cm^{-2}) indicates that the Na/Na$_3$Bi anode delivers a faster mass transfer process than that of Na foil (Fig. 5(c)). Electrochemical impedance spectroscopy (EIS, VMP3, Bio-Logic, France) is an effective method to research interface changes between electrolyte components and anodes before and after 50 cycles among Na/Cu anode, Na/bulk Na$_3$Bi anode, and Na/Na$_3$Bi anode (Figs. 5(d) and S20 in Appendix A). Before cycling, the interfacial impedances of Na/Na$_3$Bi, Na/bulk Na$_3$Bi, and Na/Cu anodes are ∼2, ∼3, and ∼25 Ω, respectively. After repetitive cycling, Na/Cu anode showed augmented interfacial impedances to 55 Ω, which is commonly observed because

of the SEI accumulation and excessive dead Na build-up; conversely, benefited from the fast Na$^+$ diffusion and a stable interface, the resistance of Na/Na$_3$Bi anode maintained low and stable (∼1.5 Ω).

The galvanostatic cycling durability for Na/Cu anode, Na/bulk Na$_3$Bi anode and Na/Na$_3$Bi anode was investigated. Fig. 6(a) shows the voltage profiles for the three anodes cycled for 2 mA·cm^{-2} along with 2 mA·h·cm^{-2}. Note that the Na/Na$_3$Bi anode exhibits low overpotential (∼10 mV) with long-life stability for over 2800 h, while the other two anodes fail in 400 h. Moreover, Na/Na$_3$Bi anode displays ∼35.5 mV of low overpotentials after 300 h at a current density of 5 mA·cm^{-2} with 5 mA·h·cm^{-2}, which is superior to those of Na/Cu and Na/bulk Na$_3$Bi anode, affirming the excellent stability of Na$_3$Bi at high rates and with deep plating/stripping behaviors (Fig. 6(b)). Top and cross view SEM images (Figs. 6(c)–(f) and S21 in Appendix A) are obtained to study the derivation of the cycling durability of Na/Na$_3$Bi anode: Smooth surface morphology and compact Na$_3$Bi-penetrated structure occur during the whole cycling, whereas increasingly uneven deposition and gradually loose structure cause the failure of Na/Cu anode in a short time. X-ray photoelectron spectroscopy (XPS, ESCALAB 250Xi, Thermo Scientific, USA) was also used to examine the SEI formed in the cycled anode (Fig. S22 in Appendix A). The C 1s spectrum can be fitted using three peaks with the binding energies of 288.2 eV (RCH$_2$ONa), 286.0 eV (C–O), and 284.8 eV (C–C and C–H), whereas the O 1s spectrum shows a corresponding peak at 535.5 eV (C–O), both of which are consistent with sodium alkoxides being the main reduction product of diglyme [57,58]. The O 1s spectrum also shows a peak at 530.9 eV (Na–O). Combining
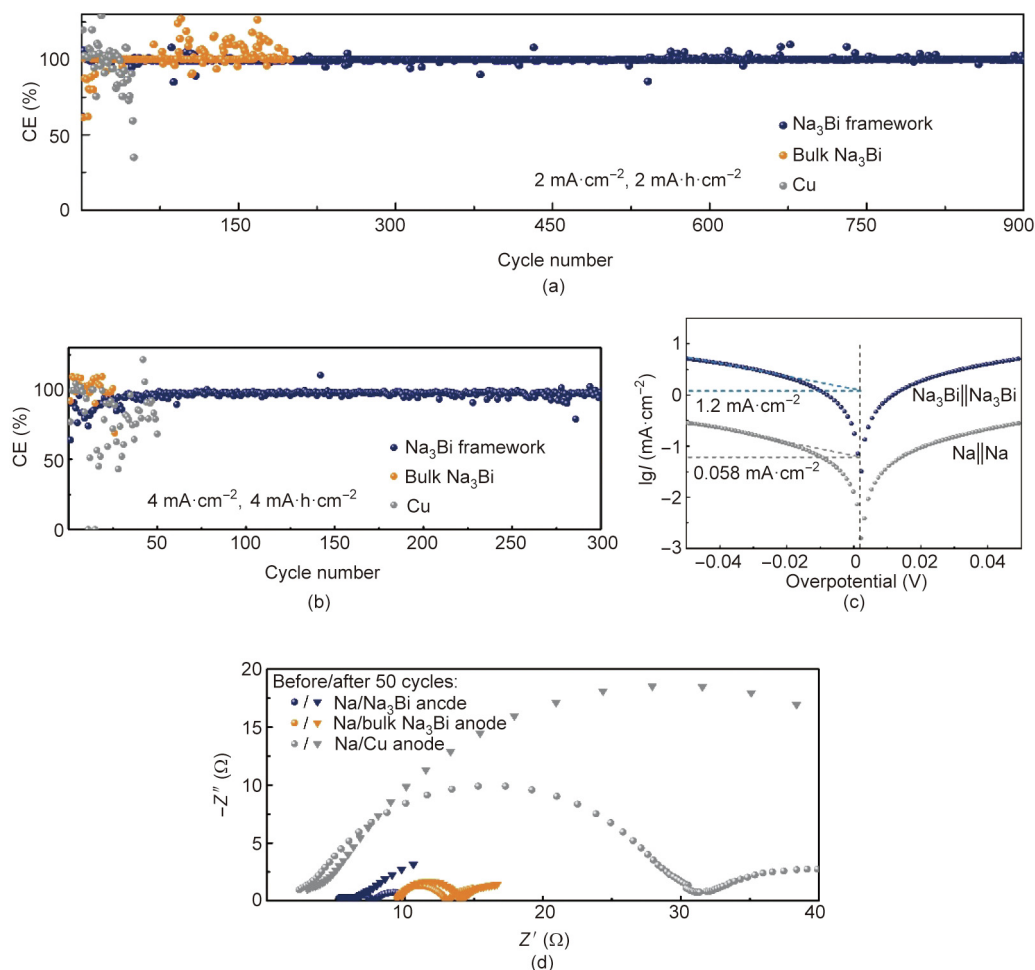
Fig. 5. The CE of Na deposition of three samples for (a) 2 mA·h·cm^{-2} and 2 mA·cm^{-2}, and (b) 4 mA·h·cm^{-2} and 4 mA·cm^{-2}. (c) Tafel plots obtained from cyclic voltammetry measurements. (d) Nyquist plot with Na/Cu electrode, Na/bulk Na$_3$Bi anode, and Na/Na$_3$Bi anode before and after 50 cycles.

these analyses with the Na 1s spectrum, we deduce that the Na 1s feature at 1071.0 eV comprises two overlapping peaks (Na–O and Na–F), which are consistent with the tabulated values for Na$_2$O and NaF. These results indicate the formation of Na$_2$O and NaOH (532.8 eV) as the reaction product of Na metal with trace amounts of O$_2$ and H$_2$O in the Ar-filled glovebox (< 0.5 ppm) and NaF as the main reduction product of NaPF$_6$ [57–59]. Overall, we see that the top surface of the SEI contained both organic (RCH$_2$ONa) and inorganic (Na$_2$O and NaF) components. Note that the electrochemical performance of Na/bulk Na$_3$Bi anode is not significantly optimized, which indirectly affirms the important role of phase-boundary diffusion in guiding homogeneous and rapid ion transport. Furthermore, the Na$_3$Bi framework remains stable based on SEM images (Fig. S23 in Appendix A) because the plating/stripping potential (±50 mV) of Na is far away from the phase change potential of Na$_3$Bi (0.7 and 0.5 V for alloying potentials and 0.6 and 0.75 V for de-alloying potentials), thus ensuring the structure's stability. The advantages of the overpotential and cycle life are also reflected in other current density and fixed real capacity conditions (Fig. S24 in Appendix A). Moreover, the Na/Na$_3$Bi anode delivers good rate performance (Fig. 6(g)), in which small polarization (∼100 mV) can still be obtained even at a relatively high current density (10 mA·cm^{-2}). It is essential to explore the performance of electrodes at low temperatures because ion-diffusion kinetics is closely related to the operating temperature, and demand for high-energy

batteries that can operate at low-temperature conditions continues to grow. The cycling performance of the Na/Na$_3$Bi and Na/Cu anodes at 2 mA·cm^{-2} and 2 mA·h·cm^{-2} at 278 K is shown in Fig. 6(h), and a Na/Na$_3$Bi anode with lower overpotential (∼100 mV) and stable cycling over 300 h is obtained. Conversely, Na/Cu anode fails quickly with 200–300 mV of overpotential, signifying that the low diffusion barrier of phase boundaries between Na and Na$_3$Bi enable effective ion transportation even at low temperature.

To assess the electrochemical performance of three different anodes in full cells, the Na/Na$_3$Bi and bare Na anodes are coupled with NVP as the cathode in 1 mol·L^{-1} NaClO$_4$ in ethylene carbonate (EC)/diethyl carbonate (DEC) respectively. Due to the fast ion transport and uniform deposition/stripping of Na/Na$_3$Bi anode, high-energy-density Na–metal batteries are obtained. NVP/(Na/ Na$_3$Bi) cell shows good capability retention of 93.8% with current densities of 0.2 to 2 C (Fig. S25 in Appendix A), which is much higher than Na anodes. As current densities increasing, the polarization of the charge/discharge plateaus slowly increases (Fig. S26 in Appendix A). Moreover, NVP/(Na/Na$_3$Bi) cell delivers excellent cycling performance for 72 mA·h·g^{-1} of reversible capacity at 1 C and over 1000 cycles, and the capacity retention is 91.1% (Figs. S25 and S26). During charging, the average CE of NVP/(Na/ Na$_3$Bi) cell at 1 C could achieve 98.35% and maintains durable cycling performance.
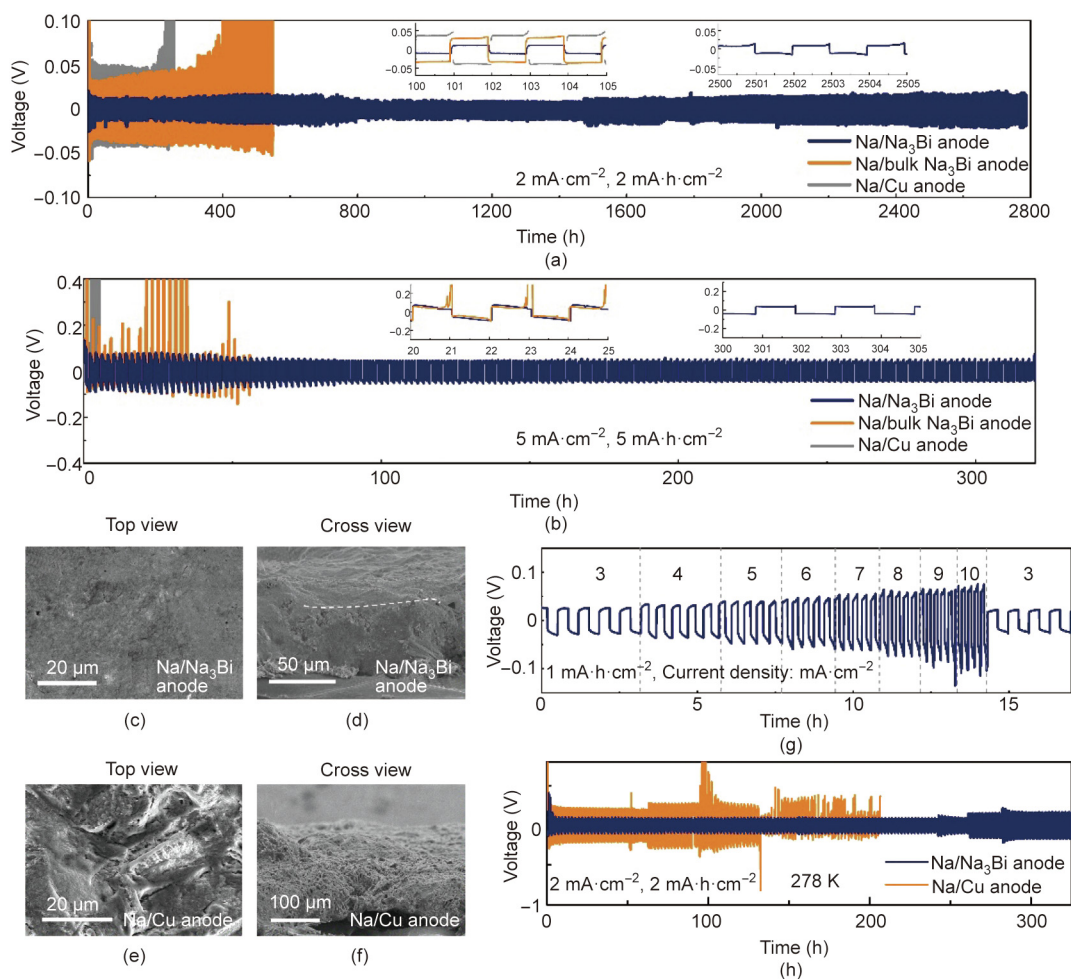
Fig. 6. Galvanostatic cycling performance of different anodes for (a) 2 mA·h·cm^{-2} and 2 mA·cm^{-2}m, and (b) 5 mA·h·cm^{-2} and 5 mA·cm^{-2}. Top and cross view SEM images of (c, d) Na$_3$Bi-penetrated Na anode and (e, f) Na/Cu anode after galvanostatic cycling. (g) Rate performance of the Na/Na$_3$Bi anode. (h) Low temperature (278 K) cycling performance of Na/Na$_3$Bi and Na/Cu anode.

3. Conclusions

In this work, bulk Na–metal anodes with sodiophilic Na$_3$Bi penetration, which holds even nucleation and uniform and dense Na deposition, could deliver a high rate, a long cycle life, and a high volumetric capacity. As a result, abundant Na/Na$_3$Bi phase boundaries, which proved to enable Na$^+$ diffusion several orders of magnitude faster than lattice diffusion, ensure sufficient and rapid Na$^+$ migration taking place upon plating and stripping. During initial deposition, the exposed "sodiophilic" Na$_3$Bi framework induces uniform local ion distribution, thereby delivering homogenous inner-space Na$^+$ plating and suppressing volume fluctuations. In subsequent stripping and plating processes, Na$^+$ rapidly exits and enters along the boundaries of Na and Na$_3$Bi phase, maintaining the stability of the anode/electrolyte interface. Furthermore, the obtained anode delivers superior cycling and rate performances coupled with the NVP cathodes.

Acknowledgments

Compliance with ethics guidelines

Wanyu Zhao, Min Guo, Zhijun Zuo, Xiaoli Zhao, Huanglin Dou, Yijie Zhang, Shiying Li, Zichen Wu, Yayun Shi, Zifeng Ma, and Xiaowei Yang declare that they have no conflict of interest or financial conflicts to disclose.

Appendix A. Supplementary data

Supplementary data to this article can be found online at https://doi.org/10.1016/j.eng.2021.08.028.

References

[1] Armand M, Tarascon JM. Building better batteries. Nature 2008;451 (7179):652–7.
[2] Whittingham MS. Lithium batteries and cathode materials. Chem Rev 2004;104(10):4271–302.
[3] Bruce PG, Freunberger SA, Hardwick LJ, Tarascon JM. Li–O$_2$ and Li–S batteries with high energy storage. Nat Mater 2012;11(1):19–29. Erratum in: Nat Mater 2012;11(2):172.
[4] Xu T, Gao P, Li P, Xia K, Han N, Deng J, et al. Fast-charging and ultrahigh-capacity lithium metal anode enabled by surface alloying. Adv Energy Mater 2020;10(8):1902343.
[5] Albertus P, Babinec S, Litzelman S, Newman A. Status and challenges in enabling the lithium metal electrode for high-energy and low-cost rechargeable batteries. Nat Energy 2018;3(1):16–21.

[6] Wu Y, Wang W, Ming J, Li M, Xie L, He X, et al. An exploration of new energy storage system: high energy density, high safety, and fast charging lithium ion battery. Adv Funct Mater 2019;29(1):1805978.

[7] Aurbach D, Levi MD, Levi E, Schechter A. Failure and stabilization mechanisms of graphite electrodes. J Phys Chem B 1997;101(12):2195–206.

[8] Zhang Y, Li J, Zhao W, Dou H, Zhao X, Liu Y, et al. Defect-free metal–organic framework membrane for precise ion/solvent separation toward highly stable magnesium metal anode. Adv Mater. In press.

[9] Yao Z, Xia X, Xie D, Wang Y, Zhou C, Liu S, et al. Enhancing ultrafast lithium ion storage of $Li_4Ti_5O_{12}$ by tailored TiC/C core/shell skeleton plus nitrogen doping. Adv Funct Mater 2018;28(31):1802756.

[10] Elango R, Demortière A, De Andrade V, Morcrette M, Seznec V. Thick binder-free electrodes for Li-ion battery fabricated using templating approach and spark plasma sintering reveals high areal capacity. Adv Energy Mater 2018;8 (15):1703031.

[11] Yang F, Mousavie SMA, Oh TK, Yang T, Lu Y, Farley C, et al. Sodium–sulfur flow battery for low-cost electrical storage. Adv Energy Mater 2018;8 (11):1701991.

[12] Liang F, Qiu X, Zhang Q, Kang Y, Koo A, Hayashi K, et al. A liquid anode for rechargeable sodium–air batteries with low voltage gap and high safety. Nano Energy 2018;49:574–9.

[13] Palomares V, Casas-Cabanas M, Castillo-Martínez E, Han MH, Rojo T. Update on Na-based battery materials. A growing research path. Energy Environ Sci 2013;6(8):2312–37.

[14] Komaba S, Murata W, Ishikawa T, Yabuuchi N, Ozeki T, Nakayama T, et al. Electrochemical Na insertion and solid electrolyte interphase for hard-carbon electrodes and application to Na-ion batteries. Adv Funct Mater 2011;21 (20):3859–67.

[15] Bai Y, Wang Z, Wu C, Xu R, Wu F, Liu Y, et al. Hard carbon originated from polyvinyl chloride nanofibers as high-performance anode material for Na-ion battery. ACS Appl Mater Interfaces 2015;7(9):5598–604.

[16] Liu P, Li Y, Hu YS, Li H, Chen L, Huang X. A waste biomass derived hard carbon as a high-performance anode material for sodium-ion batteries. J Phys Chem A 2016;4(34):13046–52.

[17] Yabuuchi N, Kubota K, Dahbi M, Komaba S. Research development on sodium-ion batteries. Chem Rev 2014;114(23):11636–82.

[18] Sun J, Lee HW, Pasta M, Yuan H, Zheng G, Sun Y, et al. A phosphorene–graphene hybrid material as a high-capacity anode for sodium-ion batteries. Nat Nanotechnol 2015;10(11):980–5.

[19] Pan H, Hu YS, Chen L. Room-temperature stationary sodium-ion batteries for large-scale electric energy storage. Energy Environ Sci 2013;6 (8):2338–60.

[20] Hwang JY, Myung ST, Sun YK. Sodium-ion batteries: present and future. Chem Soc Rev 2017;46(12):3529–614.

[21] Li Y, Lu Y, Adelhelm P, Titirici MM, Hu YS. Intercalation chemistry of graphite: alkali metal ions and beyond. Chem Soc Rev 2019;48(17):4655–87.

[22] Wang A, Hu X, Tang H, Zhang C, Liu S, Yang YW, et al. Processable and moldable sodium–metal anodes. Angew Chem Int Ed 2017;56 (39):11921–6.

[23] Zhao Y, Goncharova LV, Lushington A, Sun Q, Yadegari H, Wang B, et al. Superior stable and long life sodium metal anodes achieved by atomic layer deposition. Adv Mater 2017;29(18):1606663.

[24] Wang H, Wang C, Matios E, Li W. Facile stabilization of the sodium metal anode with additives: unexpected key role of sodium polysulfide and adverse effect of sodium nitrate. Angew Chem Int Ed 2018;57(26):7734–7.

[25] Guo M, Dou H, Zhao W, Zhao X, Wan B, Wang J, et al. Three dimensional frameworks of super ionic conductor for thermodynamically and dynamically favorable sodium metal anode. Nano Energy 2020;70:104479.

[26] Xu Z, Yang J, Zhang T, Sun L, Nuli Y, Wang J, et al. Stable Na metal anode enabled by a reinforced multistructural SEI layer. Adv Funct Mater 2019;29 (27):1901924.

[27] Zhang D, Li B, Wang S, Yang S. Simultaneous formation of artificial SEI film and 3D host for stable metallic sodium anodes. ACS Appl Mater Interfaces 2017;9 (46):40265–72.

[28] Tang S, Qiu Z, Wang XY, Gu Y, Zhang XG, Wang WW, et al. A room-temperature sodium metal anode enabled by a sodiophilic layer. Nano Energy 2018;48:101–6.

[29] Luo J, Wang C, Wang H, Hu X, Matios E, Lu X, et al. Pillared mxene with ultralarge interlayer spacing as a stable matrix for high performance sodium metal anodes. Adv Funct Mater 2019;29(3):1805946.

[30] Yang T, Qian T, Sun Y, Zhong J, Rosei F, Yan C. Mega high utilization of sodium metal anodes enabled by single zinc atom sites. Nano Lett 2019;19 (11):7827–35.

[31] Fang Y, Zhang Y, Zhu K, Lian R, Gao Y, Yin J, et al. Lithiophilic three-dimensional porous $Ti_3C_2T_x$–rGO membrane as a stable scaffold for safe alkali metal (Li or Na) anodes. ACS Nano 2019;13(12):14319–28.

[32] Zhu M, Li S, Li B, Gong Y, Du Z, Yang S. Homogeneous guiding deposition of sodium through main group II metals toward dendrite-free sodium anodes. Sci Adv 2019;5(4):eaau6264.

[33] Xu Y, Wang C, Matios E, Luo J, Hu X, Yue Q, et al. Sodium deposition with a controlled location and orientation for dendrite-free sodium metal batteries. Adv Energy Mater 2020;10(44):2002308.

[34] Guo W, Liu S, Guan X, Zhang X, Liu X, Luo J. Mixed ion and electron-conducting scaffolds for high-rate lithium metal anodes. Adv Energy Mater 2019;9 (20):1900193.

[35] Jäckle M, Helmbrecht K, Smits M, Stottmeister D, Groß A. Self-diffusion barriers: possible descriptors for dendrite growth in batteries? Energy Environ Sci 2018;11(12):3400–7.

[36] Kasemchainan J, Zekoll S, Jolly DS, Ning Z, Hartley GO, Marrow J, et al. Critical stripping current leads to dendrite formation on plating in lithium anode solid electrolyte cells. Nat Mater 2019;18(10):1105–11.

[37] Shi F, Pei A, Boyle DT, Xie J, Yu X, Zhang X, et al. Lithium metal stripping beneath the solid electrolyte interphase. Proc Natl Acad Sci USA 2018;115 (34):8529–34.

[38] Jäckle M, Groß A. Microscopic properties of lithium, sodium, and magnesium battery anode materials related to possible dendrite growth. J Chem Phys 2014;141(17):174710.

[39] O'Reilly DE. Self-diffusion of solid and liquid sodium. J Phys Chem 1974;78 (22):2275–80.

[40] Park JH, Choi YS, Byeon YW, Ahn JP, Lee JC. Diffusion kinetics governing the diffusivity and diffusion anisotropy of alloying anodes in Na-ion batteries. Nano Energy 2019;65:104041.

[41] Yurkiv V, Gutiérrez-Kolar JS, Unocic RR, Ramsubramanian A, Shahbazian-Yassar R, Mashayek F. Competitive ion diffusion within grain boundary and grain interiors in polycrystalline electrodes with the inclusion of stress field. J Electrochem Soc 2017;164(12):A2830–9.

[42] Lin D, Zhao J, Sun J, Yao H, Liu Y, Yan K, et al. Three-dimensional stable lithium metal anode with nanoscale lithium islands embedded in ionically conductive solid matrix. Proc Natl Acad Sci USA 2017;114(18):4613–8.

[43] Zhang C, Liu S, Li G, Zhang C, Liu X, Luo J. Incorporating ionic paths into 3D conducting scaffolds for high volumetric and areal capacity, high rate lithium–metal anodes. Adv Mater 2018;30(33):1801328.

[44] Wan M, Kang S, Wang L, Lee HW, Zheng GW, Cui Y, et al. Mechanical rolling formation of interpenetrated lithium metal/lithium tin alloy foil for ultrahigh-rate battery anode. Nat Commun 2020;11(1):829.

[45] Zheng X, Yang W, Wang Z, Huang L, Geng S, Wen J, et al. Embedding a percolated dual-conductive skeleton with high sodiophilicity toward stable sodium metal anodes. Nano Energy 2020;69:104387.

[46] Liu S, Deng L, Guo W, Zhang C, Liu X, Luo J. Bulk nanostructured materials design for fracture-resistant lithium metal anodes. Adv Mater 2019;31 (15):1807585.

[47] Li S, Fu J, Miao G, Wang S, Zhao W, Wu Z, et al. Toward planar and dendrite-free Zn electrodepositions by regulating Sn-crystal textured surface. Adv Mater 2021;33(21):2008424.

[48] Lu H, Xu B, Shi J, Wu M, Hu Y, Ouyang C. Structural, electronic, sodium diffusion and elastic properties of Na–P alloy anode for Na-ion batteries: insight from first-principles calculations. Mod Phys Lett B 2016;30(32–33):1650385.

[49] Han S, Park J, Lu W, Sastry AM. Numerical study of grain boundary effect on Li^+ effective diffusivity and intercalation-induced stresses in Li-ion battery active materials. J Power Sources 2013;240:155–67.

[50] Wang C, Wang L, Li F, Cheng F, Chen J. Bulk bismuth as a high-capacity and ultralong cycle-life anode for sodium-ion batteries by coupling with glyme-based electrolytes. Adv Mater 2017;29(35):1702212.

[51] Lei K, Wang C, Liu L, Luo Y, Mu C, Li F, et al. A porous network of bismuth used as the anode material for high-energy-density potassium-ion batteries. Angew Chem Int Ed 2018;57(17):4687–91.

[52] Yan K, Lu Z, Lee HW, Xiong F, Hsu PC, Li Y, et al. Selective deposition and stable encapsulation of lithium through heterogeneous seeded growth. Nat Energy 2016;1(3):16010.

[53] Fan L, Li S, Liu L, Zhang W, Gao L, Fu Y, et al. Enabling stable lithium metal anode via 3D inorganic skeleton with superlithiophilic interphase. Adv Energy Mater 2018;8(33):1802350.

[54] Li Z, Wu HB, Lou XW. Rational designs and engineering of hollow micro-/nanostructures as sulfur hosts for advanced lithium–sulfur batteries. Energy Environ Sci 2016;9(10):3061–70.

[55] Xiao J, Li Q, Bi Y, Cai M, Dunn B, Glossmann T, et al. Understanding and applying coulombic efficiency in lithium metal batteries. Nat Energy 2020;5 (8):561–8.

[56] Peng Z, Song J, Huai L, Jia H, Xiao B, Zou L, et al. Enhanced stability of Li metal anodes by synergetic control of nucleation and the solid electrolyte interphase. Adv Energy Mater 2019;9(42):1901764.

[57] Seh ZW, Sun J, Sun Y, Cui Y. A highly reversible room-temperature sodium metal anode. ACS Cent Sci 2015;1(8):449–55.

[58] Xu K. Electrolytes and interphases in Li-ion batteries and beyond. Chem Rev 2014;114(23):11503–618.

[59] Chi SS, Qi XG, Hu YS, Fan LZ. 3D flexible carbon felt host for highly stable sodium metal anodes. Adv Energy Mater 2018;8(15):1702764.